

## ENGINEERING

## An artificial sodium-selective subnanochannel

Jun Lu<sup>1†</sup>, Gengping Jiang<sup>2†</sup>, Huacheng Zhang<sup>3\*</sup>, Binbin Qian<sup>1</sup>, Haijin Zhu<sup>4</sup>, Qinfen Gu<sup>5</sup>, Yuan Yan<sup>6</sup>, Jefferson Zhe Liu<sup>6\*</sup>, Benny D. Freeman<sup>7</sup>, Lei Jiang<sup>1</sup>, Huanting Wang<sup>1\*</sup>

Single-ion selectivity with high precision has long been pursued for fundamental bioinspired engineering and applications such as in ion separation and energy conversion. However, it remains a challenge to develop artificial ion channels to achieve single-ion selectivity comparable to their biological analogs, especially for high Na<sup>+</sup>/K<sup>+</sup> selectivity. Here, we report an artificial sodium channel by subnanoconfinement of 4'-aminobenzo-15-crown-5 ethers (15C5s) into ~6-Å-sized metal-organic framework subnanochannel (MOFSNC). The resulting 15C5-MOFSNC shows an unprecedented Na<sup>+</sup>/K<sup>+</sup> selectivity of tens to 10<sup>2</sup> and Na<sup>+</sup>/Li<sup>+</sup> selectivity of 10<sup>3</sup> under multicomponent permeation conditions, comparable to biological sodium channels. A co-ion-responsive single-file transport mechanism in 15C-MOFSNC is proposed for the preferential transport of Na<sup>+</sup> over K<sup>+</sup> due to the synergetic effects of size exclusion, charge selectivity, local hydrophobicity, and preferential binding with functional groups. This study provides an alternative strategy for developing potential single-ion selective channels and membranes for many applications.

## INTRODUCTION

Biological sodium (Na<sup>+</sup>) and potassium (K<sup>+</sup>) channels with precise single-ion selectivity between Na<sup>+</sup> and K<sup>+</sup> ions play fundamental roles in almost all cell types (1). Sodium channels usually have a high Na<sup>+</sup>/K<sup>+</sup> selectivity of 30 to 500, while potassium channels has ultrahigh K<sup>+</sup>/Na<sup>+</sup> selectivity above 1000 (2, 3). The ultimate ion selectivity of these biological ion channels mainly comes from their angstrom-sized ion selectivity filters that can selectively transport one kind of ion and exclude other ions via size exclusion, electrostatic repulsion, hydrophilic-hydrophobic cooperation, and binding affinity effects (3–6). Pursuing single ion-ion selectivity with atomic-scale precision has been one of the research foci in the fields of membrane science and nanofluidics due to enormous interest in fundamental bioinspired engineering and applications such as in ion separation and electrochemical energy conversion and storage (7–10). Numerous artificial ion channels/membranes have been reported to mimic biological channels' selective ion transport properties (11–13). However, the study of artificially replicating single-ion selectivity is still in its infancy (14, 15). For example, artificial Na<sup>+</sup> and K<sup>+</sup> channels have been mainly synthesized by assembling crown ethers or other macrocycle molecules with specific Na<sup>+</sup>- or K<sup>+</sup>-binding sites into hydrophobic and soft lipid membranes (16, 17). Recently, K<sup>+</sup>-Na<sup>+</sup> selectivity has also been studied in hydrophilic solid-state nanopores with crown ethers (18–20). These channels fabricated by selective K<sup>+</sup>-binding molecules achieved moderate K<sup>+</sup>/Na<sup>+</sup> selectivity of 10 to 84; however, only a few examples of artificial ion channels have been

reported with Na<sup>+</sup>-binding molecules, and they showed a low of Na<sup>+</sup> selectivity over other ions, e.g., Na<sup>+</sup>/K<sup>+</sup> selectivity of 3 to 15 and Na<sup>+</sup>/Li<sup>+</sup> selectivity of 0.7 to 26 (21–23). Among the self-assembled channels in soft lipid membrane-based 15-crown-5 ether molecules with specific Na<sup>+</sup>-binding ability and 18-crown-6 ether (18C6) molecules with specific K<sup>+</sup>-binding ability, most of those artificial ion channels showed K<sup>+</sup> selectivity over Na<sup>+</sup> (16, 18, 24), while some 18C6-based channels showed a weak Na<sup>+</sup> selectivity over K<sup>+</sup> (25). However, in these artificial ion channels, the exact configuration and distribution of crown ethers assembled in lipid membranes or solid-state nanopores are unknown, and consequently, the detailed ion transport mechanisms remain elusive. Therefore, it remains a challenge to harness the specific ion binding properties of crown ethers to achieve high ion selectivity.

Metal-organic frameworks (MOFs), as a class of porous crystalline materials composed of metal ions/clusters and organic linkers, have been widely studied as sieving materials (26, 27). Recently, MOFs have also been shown to exhibit outstanding ion selectivity by the construction of MOF membranes and nanofluidic devices (10, 28). Because of the outstanding size sieving effect, charge selectivity and metal-acid group oxygen coordination from the well-defined nanometer to subnanometer channels, a series of MOF membranes, including UiO-66-(COOH)<sub>1–2</sub>, Hong Kong University of Science and Technology (HKUST)-1/polymer, and zeolitic imidazolate framework (ZIF)-8 membranes, have been reported for promising monovalent/divalent ion selectivity (29–33). MOF-based nanochannels (NCs) often exhibit much higher ion selectivities than other angstrom-porous membranes based on two-dimensional (2D) layered materials and polymers (34–36), showing great potential for the construction of subnanometer platforms for ion transport and separation applications (10, 37).

Here, we report a synthetic sodium channel by the assembly of 4'-aminobenzo-15-crown-5 ether (15C5) molecules in UiO-66-(COOH)<sub>2</sub> MOF subnanochannel (MOFSNC). With the specific binding of the confined 15C5 with Na<sup>+</sup> ions, the 15C5-MOFSNC shows a permeation rate sequence of Na<sup>+</sup> >> K<sup>+</sup> > Li<sup>+</sup> and an ultrahigh Na<sup>+</sup>/K<sup>+</sup> selectivity of tens to hundreds, which is comparable to its biological counterparts and one to two orders of magnitude

Copyright © 2023 The Authors, some rights reserved; exclusive licensee American Association for the Advancement of Science. No claim to original U.S. Government Works. Distributed under a Creative Commons Attribution NonCommercial License 4.0 (CC BY-NC).

<sup>1</sup>Department of Chemical and Biological Engineering, Monash University, Clayton, Victoria 3800, Australia. <sup>2</sup>Department of Applied Physics, College of Science, Wuhan University of Science and Technology, Wuhan 430072, China. <sup>3</sup>Chemical and Environmental Engineering, School of Engineering, RMIT University, Melbourne, Victoria 3000, Australia. <sup>4</sup>Institute for Frontier Materials, Deakin University Waurn Ponds Campus, Geelong, Victoria 3216, Australia. <sup>5</sup>ANSTO, Australian Synchrotron, 800 Blackburn Rd., Clayton, Victoria 3168, Australia. <sup>6</sup>Department of Mechanical Engineering, The University of Melbourne, Parkville, Victoria 3010, Australia. <sup>7</sup>Department of Chemical Engineering, The University of Texas at Austin, Austin, TX, USA.

†These authors contributed equally to this work.

\*Corresponding author. Email: huacheng.zhang@rmit.edu.au (H.Z.); zhe.liu@unimelb.edu.au (J.Z.L.); huanting.wang@monash.edu (H.W.)

higher than previously reported artificial sodium channels. Combined experiments and simulations reveal the selective ion transport mechanisms as follows: (i) The 15C5-modified MOF pores preferentially bind with  $\text{Na}^+$  strongly and favor the single file of  $\text{Na}^+$  transport while excluding  $\text{K}^+$ . (ii) Without the presence of  $\text{Na}^+$  ions,  $\text{K}^+$  can also transport through the 15C5-modified MOF pores at a high rate because of the weak binding affinity of 15C5 with  $\text{K}^+$  ions. The retarded conduction of  $\text{Li}^+$  ions can be explained by the enhanced size exclusion of the 15C5-modified MOF pores and the binding affinity of  $-\text{COOH}$  throughout the 15C5-MOFSNC. Overall, MOF-confined 15C5s function as a gatekeeper, mimicking the selectivity filter of biological sodium channels, to achieve selective  $\text{Na}^+$  transport while excluding  $\text{K}^+$  and  $\text{Li}^+$  ions. As the first example of ultrahigh single sodium ion selectivity in subnanometer porous MOF channels with well-confined specific ion binding sites, our study provides an alternative pathway to develop diverse subnanometer channels/membranes for ion separation and other emerging nanofluidic applications.

## RESULTS

### Preparation of 15C5-MOFSNC

For the synthesis of the 15C5-MOFSNC, 15C5 molecules were grafted into the  $\text{UiO-66-(COOH)}_2$ -MOFSNC through the condensation reaction between the  $-\text{NH}_2$  group of the crown ether and the

$-\text{COOH}$  group in  $\text{UiO-66-(COOH)}_2$  (Fig. 1). The  $\text{UiO-66-(COOH)}_2$ -MOFSNC was fabricated by growing  $\text{UiO-66-(COOH)}_2$  crystals into a single bullet-shaped polyethylene terephthalate NC (PET NC) after ethanediamine (EDA) modification (see Materials and Methods, fig. S1, and note S1 for more information). The resulting 15C5-modified MOFSNC was denoted 15C5-MOFSNC. The 15C5-MOFSNC has a heterogeneous structure in the axial direction. In other words, the modification of MOF with 15C5 occurs mostly at two ends (tip and base side), while a small amount of 15C5 molecules penetrate the middle MOF zone (Fig. 1B). The MOFSNC with an aperture size of  $\sim 6 \text{ \AA}$  is essential to ensure the selectivity of 15C5-MOFSNC (Fig. 1C). To better demonstrate the structure of MOFSNC and 15C5-MOFSNC, multichannel PET film (fig. S2) was used to prepare MOF NCs, and the resulting multichannel PET-MOF NC (denoted as multi-SNC) was functionalized with 15C5 molecules under the same conditions as those for single SNCs. Note that the multi-SNCs were used for structural characterization of MOFSNC and 15C5-MOFSNC, following the protocol used in previous works (32, 38). Scanning electron microscopy (SEM) images of the tip side, base side, and cross section in Fig. 2A show that the whole channel of PET NC is filled with highly intergrown MOF crystals. No cracks or grain gaps are observed as shown in the high-resolution SEM image (fig. S3). The successful growth of  $\text{UiO-66-(COOH)}_2$  within PET NC was confirmed by the powder x-ray diffraction (PXRD) patterns (Fig. 2B).

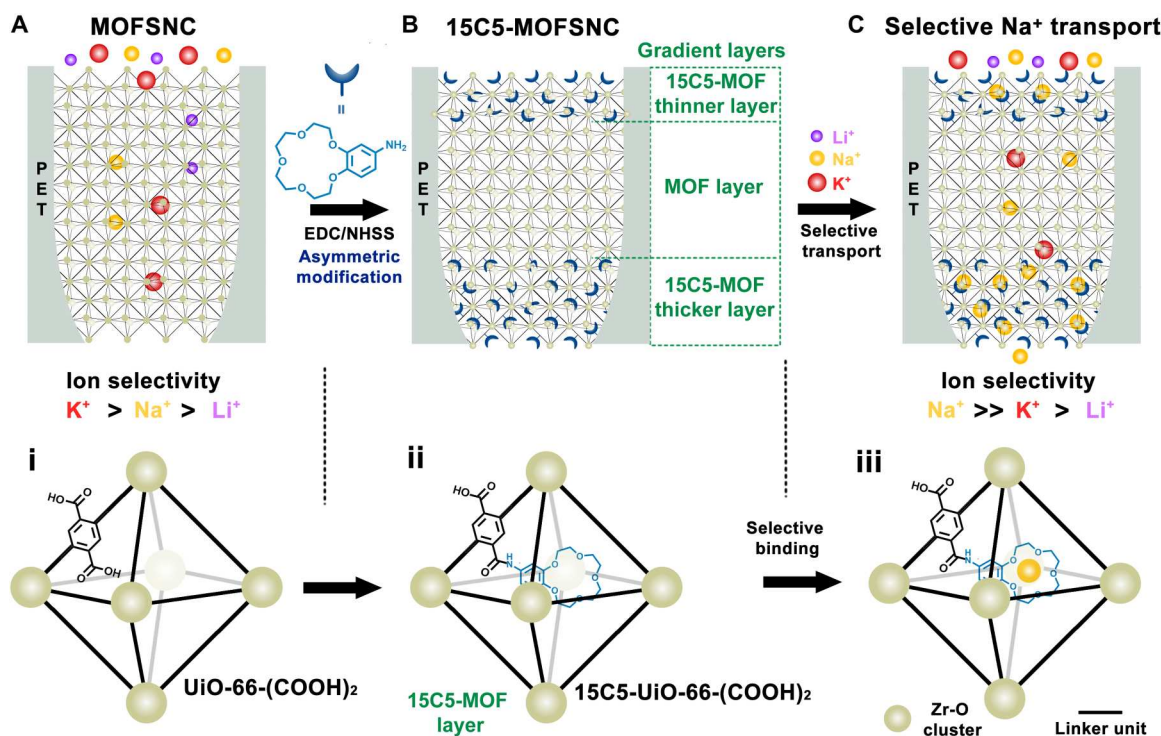


**Fig. 1. Fabrication of artificial sodium channel by assembly of 15C5 into  $\text{UiO-66-(COOH)}_2$ -based MOFSNC embedded in the single PET NC for biomimetic  $\text{Na}^+$ -selective transport.** (A) Schematic illustration of a  $\text{UiO-66-(COOH)}_2$ -based MOFSNC and the crystal structure of  $\text{UiO-66-(COOH)}_2$  (i). EDC, *N*-(3-dimethylaminopropyl)-*N'*-ethylcarbodiimide hydrochloride; NHSS, *N*-hydroxysulfosuccinimide sodium salt. (B) Schematic illustration of the 15C5-MOFSNC fabricated by grafting 15C5s into the MOFSNC and the crystal structure of 15C5- $\text{UiO-66-(COOH)}_2$  with one 15C5 in an octahedral cavity (ii). There is a gradient layer structure in the 15C5-MOFSNC: (1) a thinner 15C5- $\text{UiO-66-(COOH)}_2$  layer close to the base side; (2)  $\text{UiO-66-(COOH)}_2$  layer with negligible 15C5 in the middle zone, and (3) a thicker 15C5- $\text{UiO-66-(COOH)}_2$  layer close to the tip side. (C) Ultrasensitive  $\text{Na}^+$  transport by 15C5-MOFSNC to mimic the function of biological sodium channels and the ring of the grafted 15C5s as the selective binding sites for  $\text{Na}^+$  (iii).

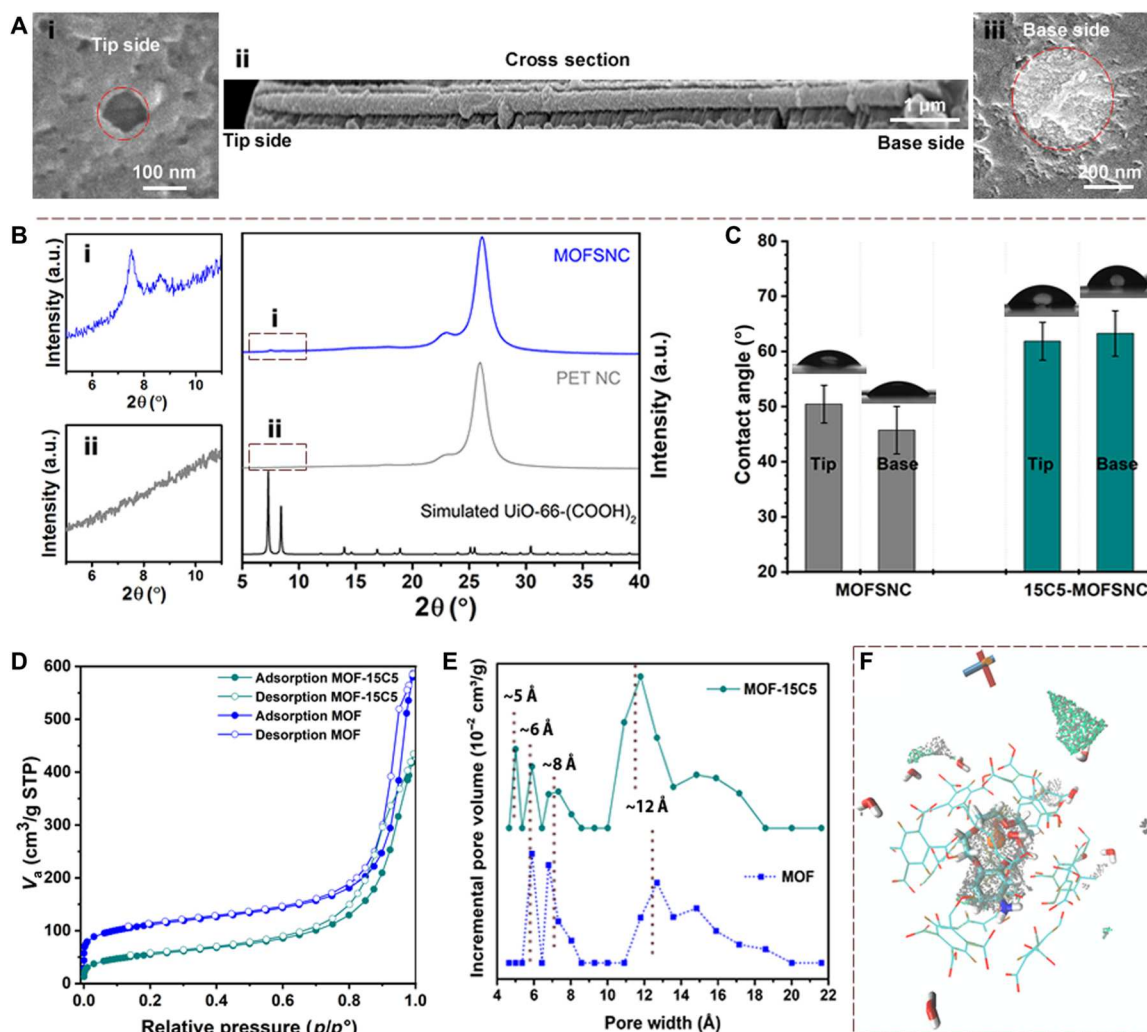


**Fig. 2. Characterization of the artificial sodium channel.** (A) SEM images of the MOFSNC: tip side surface (i), cross section (ii), and base side surface (iii). (B) PXRD of the MOFSNC and PET NC film with the  $2\theta$  range of  $5^\circ$  to  $11^\circ$  magnified as (i) and (ii). a.u., arbitrary unit. (C) Water contact angle of tip and base sides of MOFSNC and 15C5-MOFSNC. The enlarged contact angle on the top surface of 15C5-MOFSNC indicates the enhanced hydrophobicity. (D) The  $N_2$  isotherms and (E) PSDs of MOF and MOF-15C5 crystals. The reduced BET surface and pore size of MOF-15C5 indicated the narrowed aperture size of MOFSNC-15C5 compared to MOFSNC. STP, Standard Temperature and Pressure. (F) Magnified view of a single 15C5 molecule (“licorice” style) binding with a  $Na^+$  ion (orange ball) confined within an octahedral cavity of UiO-66-(COOH)<sub>2</sub> observed by MD simulations. The volume enclosed by gray surfaces is the accessible volume in UiO-66-(COOH)<sub>2</sub> supercell ( $V_{MOF}$ ). The volume enclosed by green surfaces is the volume occupied by water molecules ( $V_{H_2O}$ ). The gray region without overlapping green regions represents the volume occupied by 15C5 and cations. The filling of 15C5 molecule reduces water molecule numbers in the octahedra cavity, indicating the improved hydrophobicity of MOF channels.

No diffraction peaks appear in the pristine PET NC film (Fig. 2B, i), and the two UiO-66(COOH)<sub>2</sub> characteristic peaks at  $2\theta$  of  $7.6^\circ$  and  $8.5^\circ$  are observed in multi-SNC (Fig. 2B, ii). Energy-dispersive x-ray (EDX) mapping images and spectrum (fig. S4) of the cross section of the multi-SNC membrane demonstrate the even distribution of the main elements (Zr, C, and O) of the MOF along the axial profile of the NCs, which further supports the homogeneous structure of MOFSNC prepared by the interfacial synthesis method. All these results confirmed the successful fabrication of the UiO-66-(COOH)<sub>2</sub>-MOFSNC.

For the 15C5-MOFSNC, the introduction of 15C5 molecules endows both chemical functionalization and reduction in aperture size of the MOFSNC, which is beneficial for ion selectivity. Considering the high intergrowth of MOFSNC and the 6-Å-sized channels,

the functionalization of MOFSNC with 15C5 is not complete throughout the whole MOF structure inside the PET channel due to limited penetration of 15C5 molecules. In other words, the 15C5-MOFSNC has a heterogeneous structure, i.e., 15C5-MOF layers exist at two ends, while the MOF in the middle is less likely functionalized by 15C5, as simplistically shown in Fig. 1B. To reveal the chemical structure of 15C5-MOFSNC, we conducted the EDX elemental analysis of the cross-section of multiple 15C5-MOFSNC membrane in order to qualitatively demonstrate the profile of 4'-aminobenzon-15-crown-5 throughout the 15C5-MOFSNC. As shown in fig. S5, the N/Zr ratio in the axial direction of the cross-section of 15C5-MOFSNC is greatly dependent on the depth from the top surface. Generally, the N/Zr ratio decreases gradually with increasing the depth from both PET membrane surfaces (i.e., tip

side and base side surfaces) further to the inside, which confirms the proposed heterogeneous layer structure of 15C5-MOFSNC. The contact angle of 15C5-MOFSNC increased from  $\sim 45^\circ$  to above  $65^\circ$  on both the tip and base sides after crown ether modification (Fig. 2C), indicating the slightly enhanced hydrophobicity for the 15C5-MOF layers on the two ends. In addition, a 1 V forward voltage was applied to the base side to drive the 15C5 molecules to enter and penetrate the MOFSNC. As a result, the 15C5-MOF layer on the base side should be thicker than that on the tip side of 15C5-MOFSNC. Because of the difficulty in direct measurement of the pore size of the 15C5-MOFSNC with a heterogeneous structure inside the PET channel, we prepared MOF-15C5 particles by modifying MOF with 15C5 (note S1) to qualitatively characterize the aperture size of 15C5-MOFSNC. The fourier transform infrared spectroscopy (FTIR) and  $C^{13}$  nuclear magnetic resonance (NMR) spectra in MOF-15C5 particles show N—H, C—H, C=C, and C—O—C stretching bands and  $-\text{CH}_2-\text{CH}_2-\text{O}$  peak, respectively, indicating the successful modification of the MOF particles with crown ether (fig. S6, A and B). As shown in Fig. 1 (D and E), the Brunauer-Emmett-Teller (BET) surface area of MOF-15C5 markedly decreases to  $200.5 \text{ m}^2 \text{ g}^{-1}$  from the original value of  $409.1 \text{ m}^2 \text{ g}^{-1}$  for  $\text{UiO}-66-(\text{COOH})_2$  particles. The pore size distribution (PSD) clearly shows a peak at  $\sim 5 \text{ \AA}$ , arising from the triangle window pores grafted with 15C5 molecules, which further confirms the narrowed aperture size of the 15C5-MOF layers in 15C5-MOFSNC. Furthermore, the synchrotron PXRD results of the  $\text{UiO}-66-(\text{COOH})_2$  crystals before and after 15C5 modification in both dry and wet states and the XRD results of the pristine MOFs treated in different electrolyte solutions for 2 weeks demonstrate the high water stability of the MOF crystal structures (fig. S6, C to E). In addition, the pristine  $\text{UiO}-66-(\text{COOH})_2$  has a BET surface area comparable to the theoretical accessible surface area in the literature ( $409.1$  to  $428 \text{ m}^2 \text{ g}^{-1}$ ), and there is no broad PXRD peak at  $2\theta$  of  $5^\circ$  to  $6^\circ$  (fig. S6, C to E) that corresponds to the cluster-missing defects (39, 40), which indicates the presence of negligible crystal defects.

Note that it is desirable to quantify the exact amount of crown ether confined in MOFSNC to better understand the ion conduction behavior, but it is challenging to precisely determine the number of 15C5 molecules in 15C5-MOFSNC, as also encountered in previously reported artificial ion channels constructed by encapsulation or self-aggregation of crown ether molecules in diverse substrates (16, 19, 41). In this work, we estimated the average amount of

15C5 grafted in MOFSNC by a combination of molecular dynamics (MD) simulations and experimental measurements (notes S1 and S2). The number of 15C5 molecules in the MOF-15C5 particles was estimated by EDX analysis to be between 1.4 and 0.6 15C5s per octahedral cavity with an average value of  $1.0 \pm 0.2$  (fig. S7), which is close to 0.88 15C5s per octahedral cavity obtained by thermogravimetric analysis (fig. S8). This is also consistent with the theoretical value obtained by matching the change in specific surface area from MD simulations with the experimental BET surface area after functionalization with 15C5 determined by the  $\text{N}_2$  sorption technique (figs. S9 and S10). Figure 2F shows the magnified view of a single 15C5 molecule binding with  $\text{Na}^+$  within one octahedral cavity of  $\text{UiO}-66-(\text{COOH})_2$ . After one 15C5 binds with one  $\text{Na}^+$ , the space of the octahedral cavity is largely occupied, and the cation is partially dehydrated because there is not much space in the cavity for hydration shells (Fig. 2F and figs. S11 and S12). As a result, the cross-sectional structure of the 15C5-MOFSNC was composed of the hydrophobic 15C5-MOF layer (tip)—the hydrophilic MOF zone—the hydrophobic 15C5-MOF layer (base), as shown in Fig. 1B. The confined large 15C5 molecules act as the gatekeepers of the MOFSNC, while residual  $-\text{COOH}$  and deprotonated  $-\text{COO}^-$  groups on the MOF channels also facilitate metal ion transport in the MOFSNC (32). Additional MD simulations also reveal that the 15C5 molecules confined within MOFSNC could preferentially bind with  $\text{Na}^+$  over  $\text{K}^+$  (note S2.1 and fig. S12).

### Ion selectivity performance of 15C5-MOFSNC

The ion-selective properties of 15C5-MOFSNC and MOFSNC were first investigated by multicomponent permeation experiments. A feed solution prepared by mixing equal molar amounts of 1.0 M KCl, 1.0 M NaCl, and 1.0 M LiCl was added to the base side of the SNC membrane (Fig. 3A), while the tip side was filled with Milli-Q water. A constant voltage of 1.0 V was applied on the base side of the membrane for 24 hours to drive ion permeation through the SNCs. The metal ion concentrations in the permeate side were determined by inductively coupled plasma optical emission spectrometry and mass spectrometry (ICP-OES/MS), and the ion permeation rates and ratios were then calculated on the basis of the concentrations to determine the ion permeability and selectivity of the MOFSNCs. The observed ion permeation rates of the MOFSNC followed the order of  $\text{K}^+ > \text{Na}^+ > \text{Li}^+$  ranging from  $10^{-3}$  to  $10^{-2} \text{ mol m}^{-2} \text{ hour}^{-1}$  (Fig. 3B) due to their differences in both

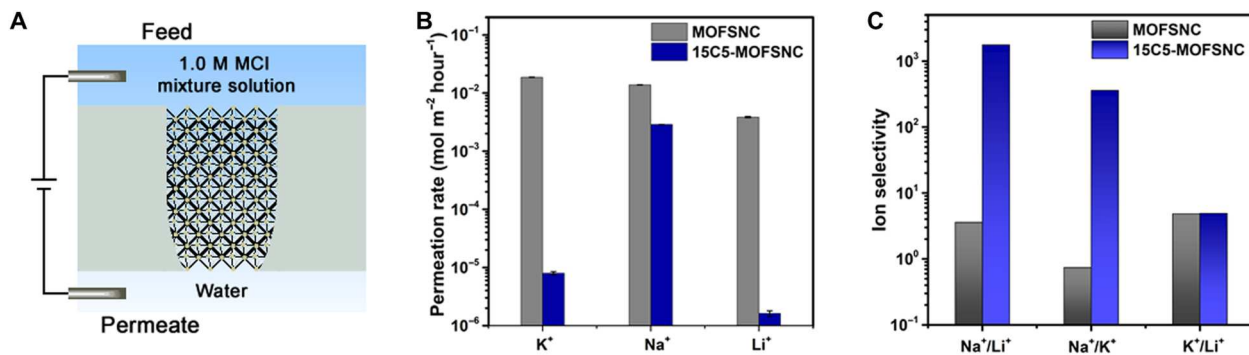


**Fig. 3. Ion permeation rate and selectivity of MOFSNC and 15C5-MOFSNC.** (A) Schematics of the experimental setup for ion permeation under multicomponent conditions where a transmembrane voltage is applied to drive ion transport from the feed (base side) to the permeate side (tip side). (B and C) Permeation rate and selectivity of the MOFSNC and 15C5-MOFSNC in multicomponent solutions with an applied voltage bias of 1.0 V.

hydration diameter and binding affinity with the carboxylic groups of MOFSNC. In contrast, the 15C5-MOFSNC exhibited ultrasensitive sodium conduction over  $K^+$  and  $Li^+$  (Fig. 3, B and C), which can be attributed to the specific binding effect between  $Na^+$  ions and the introduced 15C5 molecules (Fig. 1C). Specifically, the permeation rate of  $Na^+$  was up to  $2.87 \times 10^{-3} \text{ mol m}^{-2} \text{ hour}^{-1}$ , while those for  $K^+$  and  $Li^+$  were  $7.98$  and  $1.62 \times 10^{-6} \text{ mol m}^{-2} \text{ hour}^{-1}$ , respectively (Fig. 3B). Correspondingly, the mixed  $Na^+/K^+$  and  $Na^+/Li^+$  selectivity 15C5-MOFSNC was up to 360.1 and 1770.0, respectively, much higher than those (i.e., 0.74 and 3.59) of the MOFSNC (Fig. 3C). We also tested four different 15C5-MOFSNC samples to demonstrate the variation of ion selectivity, and the  $Na^+/K^+$  selectivity ranged from 282.9 to 620.6, while  $Na^+/Li^+$  selectivity was between 971.6 and 2248.6, as shown in fig. S13. The ultrahigh  $Na^+/K^+$  selectivity observed in the 15C5-MOFSNC is comparable to the ultimate selectivity of biological sodium channels and among of the highest values achieved by previously reported artificial sodium channels (table S1).

Further ion permeation experiments under a wide range of applied voltages from 0.25 to 4.0 V demonstrated the robust  $Na^+$  selectivity of 15C5-MOFSNC. As shown in Fig. 4 (A and B), the permeation rates for all three monovalent metal ions increased gradually with an applied voltage below 1.0 V. With a higher applied voltage, the  $Na^+$  permeation rate increased slightly, while the  $Li^+$

and  $K^+$  permeation rates increased much more markedly. As a result, both  $Na^+/K^+$  and  $Na^+/Li^+$  selectivity could maintain higher values at a low voltage bias range of below 1.0 V, and they decreased gradually with further increasing voltage bias. Specifically, the  $Na^+/K^+$  selectivity decreased to  $\sim 160$  and  $Na^+/Li^+$  dropped to  $\sim 900$  at 4.0 V (Fig. 4B). All above ion selectivities were obtained with a feed pH value of  $5.8 \pm 0.2$ . To further study the effect of the surface charge on the single ion selectivity, we also carried out ion permeation experiments at different pH values (Fig. 4C). Generally, the preferential  $Na^+$  permeation rate decreased with decreasing pH value, while the  $K^+$  followed a reversed trend. Therefore, a high pH value is essential for 15C5-MOFSNC to maintain  $Na^+/K^+$  selectivity at  $10^2$ , and at a low pH of 3.1,  $Na^+/K^+$  selectivity was 41.2.  $Na^+/Li^+$  selectivity showed a similar trend with variation of pH value. This pH-dependent ion selectivity can be explained by the charge selectivity of 15C5-MOFSNC. As discussed in our earlier work (32), good charge selectivity can be obtained at higher pH values above the isotropic point of  $-\text{COOH}$  (e.g.,  $\sim 3$ ) due to the deprotonation of  $-\text{COOH}$  groups in  $\text{UiO-66}-(\text{COOH})_2$ , which has been reported as an ion sieving mechanism for biological ion channels. These results confirm that we successfully prepared an artificial sodium channel with ultrahigh ion selectivity by confining a crown ether into angstrom-sized MOFSNC.

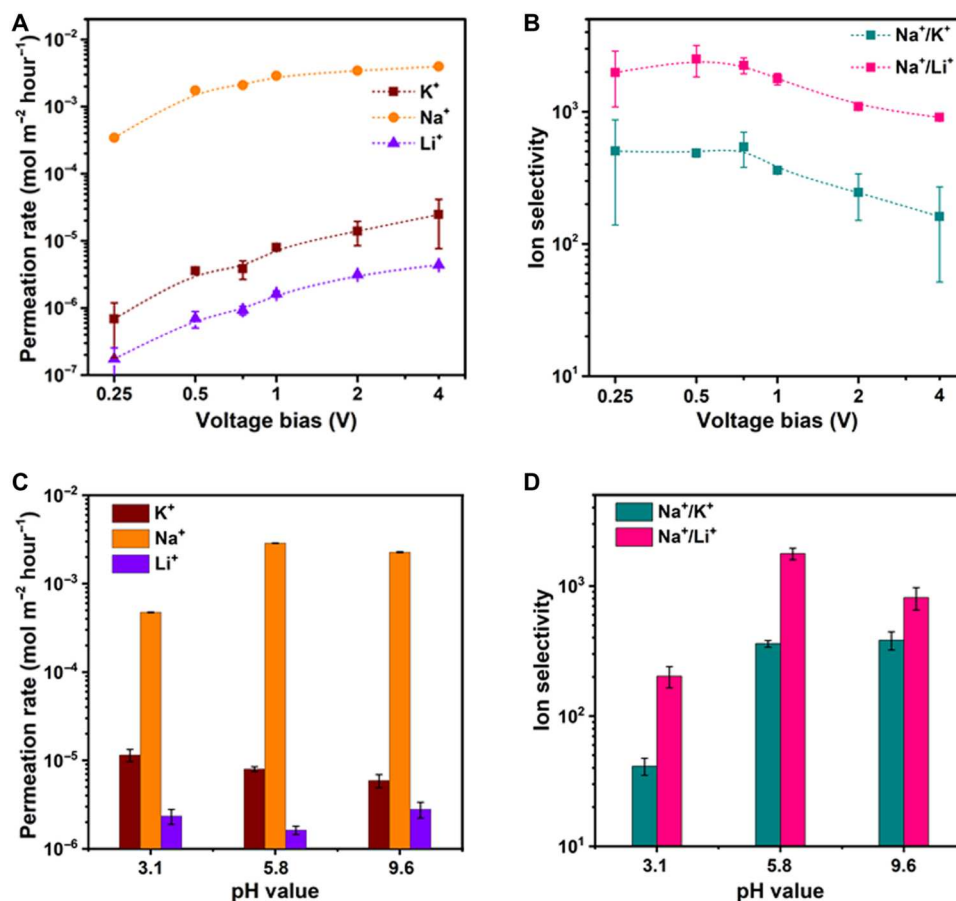


**Fig. 4. Ultrahigh  $Na^+$  selectivity of 15C5-MOFSNC.** (A) Permeation rates of 15C5-MOFSNC with applied voltage bias of 0.25 to 4.0 V. (B) Ion selectivity of 15C5-MOFSNC with applied voltage bias of 0.25 to 4.0 V. (C) The variation of ion selectivity with pH value. (D) Cycling stability of 15C5-MOFSNC ultrahigh ion selectivity.

## Insights into the ion selectivity mechanisms of 15C5-MOFSNC

As previously reported, some ion channels assembled by 15C5 molecules showed  $K^+$  selectivity over  $Na^+$  (16, 24), we further conducted current-voltage relation ( $I$ - $V$ ) tests and single-component permeation experiments for the 15C5-MOFSNC and MOFSNC to better elucidate the underlying ion selective mechanisms. Compared to symmetric  $I$ - $V$  curves for MOFSNC,  $I$ - $V$  curves of 0.1 M KCl and NaCl for 15C5-MOFSNC showed an obvious rectifying effect (Fig. 5, A and B), confirming the acquired heterogeneous structure of the 15C5-MOFSNC (Fig. 1B). In addition, this also indicates that the 15C5-MOFSNC can quickly transport  $K^+$  and  $Na^+$  in a single-component solution. Furthermore, ion permeation experiments were carried out with a single-component solution of 1 M KCl, 1 M NaCl, or 1 M LiCl used as the feed in the base side of the membrane (Fig. 5C). As shown in Fig. 5C, the ion permeation rate follows the order of  $K^+ > Na^+ \gg Li^+$ , consistent with the current value order of  $I$ - $V$  curves at positive voltage bias, and the ideal  $Na^+/K^+$  and  $Na^+/Li^+$  selectivity was calculated to be 0.83 and 592.2, respectively. These results demonstrate that under single-component conditions, the 15C5-MOFSNC can have dual  $Na^+$ - and  $K^+$ -selective transport properties, mimicking the functionalities of biological NaK channels (42, 43), while the transport of  $Li^+$  ions in 15C5-MOFSNC can be greatly excluded, i.e., high  $Na^+/Li^+$  selectivity was concordantly achieved under both single-component and multiple-component conditions. In contrast, under multiple-component conditions, the 15C5-MOFSNC exhibited the ultrahigh

selective transport order of  $Na^+ \gg K^+ > Li^+$ . Therefore, it is reasonable to propose that there exist different ion sieving mechanisms for  $Na^+/K^+$  and  $Na^+/Li^+$  selectivity in 15C5-MOFSNC.

We proposed that the above ion conductive behavior mimicking biological sodium channels may come from ion-specific conductive mechanisms in 15C5-MOFSNC. The hindered transport of  $Li^+$  ions in 15C5-MOFSNC can be mainly attributed to the enhanced size exclusion effect, as verified by the reduced aperture size of  $\sim 5 \text{ \AA}$  of 15C5-MOFSNC from  $\sim 6 \text{ \AA}$  of MOFSNC (Fig. 5D). The hydrated diameter of  $Li^+$  is  $7.56 \text{ \AA}$ , much higher than those of  $Na^+$  ( $7.12 \text{ \AA}$ ) and  $K^+$  ( $6.62 \text{ \AA}$ ). This aperture size of 15C5-MOFSNC is much smaller than the hydrated diameter of  $Li^+$  ( $\sim 5.0 \text{ \AA}$  versus  $7.76 \text{ \AA}$ ), indicating that there is much energy barrier that  $Li^+$  must counter before entering and pass through the 15C5-MOFSNC. As a result, the transport rate of  $Li^+$  is much lower than that of the other two ions. In contrast, there is a facilitated transport mechanism for the preferential  $Na^+$  transport in 15C5-MOFSNC (Fig. 6A). 15-crown-5 ether is well known for its specific binding affinity for  $Na^+$  ions. In this case, the 15C5s modified on the outer surface of MOFSNC tend to selectively bind with  $Na^+$ , favoring the dehydration of  $Na^+$  in the pore mouth of 15C5-MOF layers, despite the greater hydration diameter of  $Na^+$  than aperture size of 15C5-MOFSNC. Once they enter the 15C5-MOFSNC, the  $Na^+$  ions undergo a repeated rehydration-dehydration process to transport throughout the 15C5-MOFSNC. Likewise, the 15C5s confined within the 15C5-MOF layer also promote the dehydration of  $Na^+$  within 15C5-MOFSNC. Under applied voltage bias, the improved

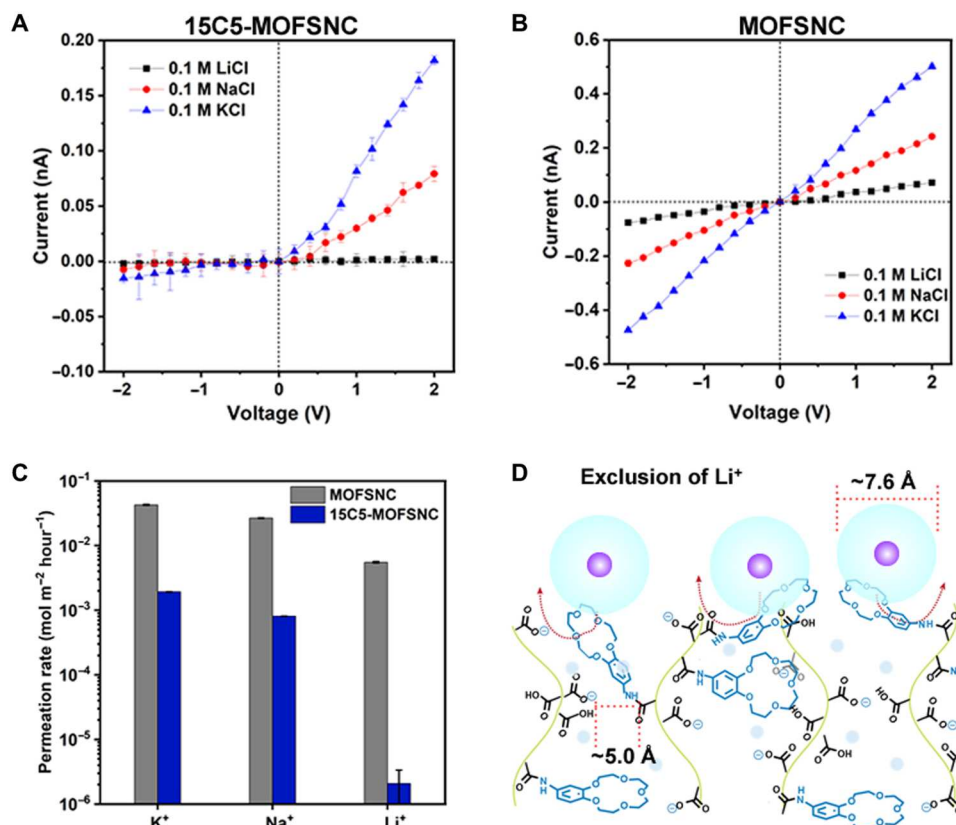


**Fig. 5. Understanding of the ion selectivity mechanisms of 15C5-MOFSNC.** (A)  $I$ - $V$  curves of the 15C5-MOFSNC. (B)  $I$ - $V$  curves of the MOFSNC. (C) Permeation rates of 15C5-MOFSNC and MOFSNC in single-component solutions with an applied voltage bias of 1.0 V. (D) Schematic diagram of retarded  $Li^+$  transport in 15C5-MOFSNC.

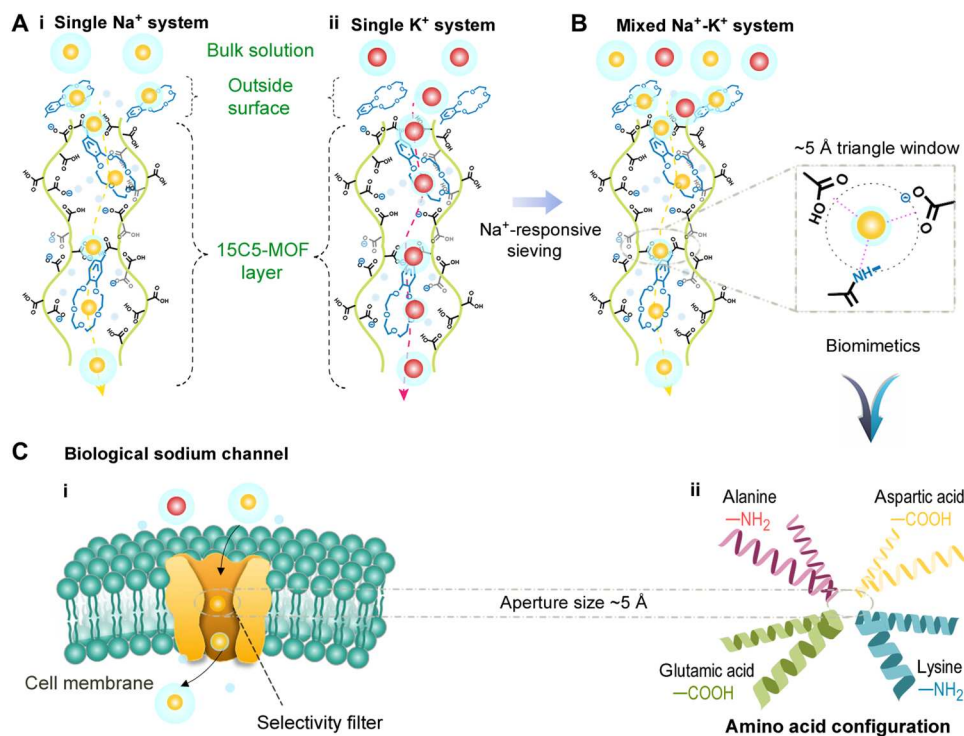


**Fig. 6. Biomimetic ion selectivity mechanisms of 15C5-MOFSNC.** (A) Preferential transport for Na<sup>+</sup> (i) and K<sup>+</sup> (ii) in 15C5-MOF layers of 15C5-MOFSNC in single-component solutions. (B) Preferential transport for Na<sup>+</sup> against K<sup>+</sup> in 15C5-MOF layers of 15C5-MOFSNC in mixed solutions. The coordination of Na<sup>+</sup>-functional groups in the triangle window plane is highlighted in the dashed rectangle. Preferential binding of the 15C5 with Na<sup>+</sup> leads to the exclusion of both K<sup>+</sup> and Li<sup>+</sup> under the multicomponent solution, which functions as the biological Na<sup>+</sup> selectivity filter. (C) Biological sodium channel with the selectivity filter (i) as the inspiration for the biomimetic design of artificial sodium channels. The configuration of amino acids (ii) is highlighted to demonstrate the essential role of Na<sup>+</sup>-functional group coordination for Na<sup>+</sup>/K<sup>+</sup> selectivity.

hydrophobicity, as confirmed by experiment and simulations (Fig. 2, C and F), can also favor the dehydration of Na<sup>+</sup>. All these will contribute to the reduced energy required for Na<sup>+</sup> dehydration and lastly the fast transport of Na<sup>+</sup> over Li<sup>+</sup> in 15C5-MOFSNC. Different from the strong binding affinity with Na<sup>+</sup>, 15-crown-5 ethers can have weak binding affinity with K<sup>+</sup>. We proposed that there should be a similar facilitated transport mechanism for K<sup>+</sup> in 15C5-MOFSNC in single-component systems, resembling that for Na<sup>+</sup> (Fig. 6B). The difference lies in that the moderate binding of K<sup>+</sup> with the 15C5 ring does not entail as a high dehydration degree for K<sup>+</sup> as Na<sup>+</sup>, also because of the smaller hydration diameter of K<sup>+</sup>. This can explain the slightly higher conduction for K<sup>+</sup> than Na<sup>+</sup> in single-component systems, as evidenced by the K<sup>+</sup>/Na<sup>+</sup> selectivity from earlier synthetic ion channels constructed by 15-crown-5 ethers embedded in liquid lipid membranes (18, 24). However, when both Na<sup>+</sup> and K<sup>+</sup> are present simultaneously in the feed, their facilitated transport manners in 15C5-MOFSNC will compete against each other, which leads to the exclusively Na<sup>+</sup>-facilitated transport, as shown in Fig. 6C. It is proposed that a higher binding affinity tends to result in a higher ion concentration in the local zone, i.e., the concentration of Na<sup>+</sup> is higher than that of K<sup>+</sup> in the 15C5-MOF layers. To verify this, ion adsorption experiments on MOF and 15C5-MOF particles with the mixed ion solutions further demonstrated the competing adsorption capacity K<sup>+</sup> versus Na<sup>+</sup> of 15C5-MOF (note S1). Fig. S14 shows that 15C5-MOF exhibited a higher adsorption capacity for Na<sup>+</sup> (3.92 mmol g<sup>-1</sup>) than for K<sup>+</sup>

(2.22 mmol g<sup>-1</sup>) and Li<sup>+</sup> (2.34 mmol g<sup>-1</sup>). Therefore, the presence of higher concentration of Na<sup>+</sup> can preferentially occupy the binding sites otherwise left for K<sup>+</sup> and then favor Na<sup>+</sup> conduction, which to some extent mimics the “knock-on” mechanisms in biological ion channels (44, 45). In other words, the 15C5-MOFSNC exhibited ion-responsive sieving mechanism, i.e., the presence of Na<sup>+</sup> depresses K<sup>+</sup> transport, which has never been reported before. Moreover, in the 15C5-MOF layers, the presence of one -COOH, one -CONH-, and another -COOH in the triangle window plane (dashed rectangle in Fig. 6B) resembles, to some extent, the configuration of amino acids (with end groups of -NH<sub>2</sub> and -COOH groups) in the selectivity filters of biological sodium channels (Fig. 6C). This functional group configuration may form Na<sup>+</sup>-functional group coordination to further favor the facilitated Na<sup>+</sup> transport, mimicking the influencing factor proposed for biological sodium channels (6). As a result, Na<sup>+</sup> ions tend to be almost fully dehydrated to become almost “naked” Na<sup>+</sup> to tightly approach the ~2.2-Å-sized 15C5 ring and skim through or even pass through in a single-file manner, analogous to the “knock-on” mechanism in KcsA ion channels.

Moreover, comprehensive theoretical simulations by combining MD simulation, density functional theory (DFT) calculations, and the well-established modified Poisson-Nernst-Planck (mPNP) theory (46) were further conducted to confirm the mechanisms for Na<sup>+</sup>-selective transport in 15C5-MOFSNC under mixed solution conditions (note S2 and figs. S16 to S23). MD simulations

showed a stronger  $\text{Na}^+$  binding over  $\text{K}^+$  (0.076 versus 0.0053 eV) onto a single 15C5 molecule (fig. S16A), consistent with the higher  $\text{Na}^+$  adsorption capacity in 15C5-MOF crystals (fig. S14) and DFT results (fig. S15). The preferential binding (described using the ion-specific binding potential  $\phi_{\text{Na}^+}$ ) is essential for the  $\text{Na}^+$ -facilitated transport in the mPNP model. In addition, the non-specific electrostatic adsorption by the deprotonated  $-\text{COOH}$  groups is also considered, which leads to a higher cation concentration inside the pristine  $\text{UiO-66}-(\text{COOH})_2$  framework as  $n_{\text{MOF}}^0 = 2.57 \text{ M}$  (32). Then, a 1D continuum mPNP model (fig. S16B) was established to simulate the selective ion transport in 15C5-MOFSNC (details seen in the "Simulation methods" section). The blue trapezoidal curve  $p_{15\text{C5}}(x)$  describes the nonuniform distribution of 15C5 groups in the 15C5-MOFSNC channel (seen in the "Simulation methods" section). Then, the distribution profile of  $-\text{COOH}$  groups in the 15C5-MOFSNC channel is represented by the green curve  $p_{\text{COOH}}(x)$  where the grafting of 15C5 by the condensation reaction decreases the amount of free  $-\text{COOH}$  group in 15C5-MOFSNC. To be consistent with the higher  $\text{K}^+$  current and flux values than  $\text{Na}^+$  under the single-component condition (Fig. 5, A and C), the diffusion coefficients of ions are fixed with  $D_{\text{K}^+} > D_{\text{Na}^+}$ . Note that our model focuses on the origin of switching ion selectivity. When confined into a nanoscale dimension, this specific binding interaction of crown ether with the matched ion could be enhanced (47), which can be described by increasing binding potential values (i.e.,  $\phi_{\text{Na}^+} > 0.076 \text{ eV}$ ) in the 1D 15C5-MOFSNC model. To estimate the proper  $\phi_{\text{Na}^+}$  range in our model, the variation in the concentrations  $\text{K}^+$ ,  $\text{Na}^+$ , and  $\text{Cl}^-$  with increasing  $\phi_{\text{Na}^+}$  value was studied, as shown in Fig. 7 (A and B). When  $\phi_{\text{Na}^+}$  increased to 0.15 eV, the concentration of  $\text{Cl}^-$  started to surpass the  $\text{K}^+$  concentration in 15C5-MOFSNC. The binding potential values can be as high as 0.25 eV, which can also be justified by normalized  $\text{Na}^+$  flux of a single NaCl solution being close to that of the NaCl-KCl mixed solution almost at this binding strength value range as shown in Fig. 7C, considering that the experimental  $\text{Na}^+$  permeation rate of the mixed ion solution (Fig. 3B) is slightly lower than that in a single NaCl solution (Fig. 5C). The inverse selectivity from preferential  $\text{K}^+$  transport under the single-component condition to the preferential  $\text{Na}^+$  selectivity in the NaCl/KCl mixed condition can be observed with a  $\phi_{\text{Na}^+}$  value above 0.025 eV. At the proper  $\phi_{\text{Na}^+}$  range determined (between 0.076 and 0.15 eV), a higher  $\text{Na}^+/\text{K}^+$  flux ratio (i.e.,  $\text{Na}^+/\text{K}^+$  selectivity) up to 10 can be obtained. Increasing 15C5 groups in the feed side [i.e.,  $p_{15\text{C5}}(0)/p_{15\text{C5}}(L_{\text{MOF}})$  increases from 1/10 to 1] can enhance the  $\text{Na}^+/\text{K}^+$  selectivity up to two orders of magnitude (Figs. 3 and 4). A fully 15C5-modified model leads to a selectivity of  $\sim 300$  at the upper bound of  $\phi_{\text{Na}^+}$ , which is close to our experimental results. In addition, the calculated average  $\text{Na}^+$  concentration ranged from 1.88 to 2.30 M (Fig. 7D), corresponding to 1.3 to 1.6  $\text{Na}^+$  in each cavity. Hence, all the 15C5 gated windows are occupied by  $\text{Na}^+$  ions that can be specifically released by the following  $\text{Na}^+$  ions, which is consistent with the knock-on effect shown in Fig. 6B.

## DISCUSSION

In summary, we have fabricated a  $\text{UiO-66}-(\text{COOH})_2$ -based MOFSNC with confined 15C5 to achieve high  $\text{Na}^+$  selectivity over  $\text{K}^+$  and  $\text{Li}^+$ . The  $\text{Na}^+/\text{K}^+$  selectivity of the 15C5-MOFSNC is

as high as tens to  $10^2$ , close to the highest  $\text{Na}^+/\text{K}^+$  selectivity of biological  $\text{Na}^+$  channels, and one to two orders of magnitude higher than the  $\text{Na}^+/\text{K}^+$  selectivity of previously reported artificial sodium channels. The high single-ion selectivity observed in these 15C5-MOFSNCs mainly arises from the well-arranged ion pathways formed by subnanoconfined 15C5 in MOFSNC. Functioning like selectivity filters of biological ion channels, each confined 15C5 molecule inside MOFSNCs could preferentially bind with  $\text{Na}^+$  ions and exclude  $\text{K}^+$  ions, enabling highly selective  $\text{Na}^+$  transport in multi-component solutions. Moreover, in the absence of  $\text{Na}^+$  ions, the 15C5-MOFSNC shows fast  $\text{K}^+$  conduction because each  $\text{K}^+$  could bind with two adjacent 15C5s on MOF pore windows. The ion selectivity and ion transport properties observed in MOF-confined crown ether will inspire further experimental and theoretical research on subnanoconfined ion transport. More work needs to be done in the future to further reveal the more detailed ion transport mechanisms. Our work may inspire more avenues to develop porous framework material-based biomimetic ion channels with ion-selective properties comparable to those of biological counterparts for nanoionics, ion-selective electrodes, and advanced energy and separation devices.

## MATERIALS AND METHODS

### Chemicals and materials

Zirconium (IV) chloride ( $\text{ZrCl}_4$ ), 1,2,4,5-benzenetetracarboxylic acid ( $\text{H}_4\text{BTEC}$ ), lithium chloride ( $\text{LiCl}$ ), sodium chloride ( $\text{NaCl}$ ), potassium chloride ( $\text{KCl}$ ), 15C5, sodium dodecyl diphenyl oxide disulfonate, formic acid ( $\text{HCOOH}$ ), and hydrochloric acid ( $\text{HCl}$ ) were purchased from Sigma-Aldrich. Methanol and sodium hydroxide ( $\text{NaOH}$ ) were purchased from Merck. PET membranes were purchased from Hostaphan RN12 Hoechst. It is noted that all ion selectivity studies of PET NC and MOFSNC by  $I$ - $V$  tests and ion permeation experiments of MOFSNC and 15C5-MOFSNC were conducted using single-channel ones, and multichannel membranes prepared under the same conditions were used to conduct SEM images, PXRD patterns, and contact angles of the SNCs before and after MOF modification and 15C5 modification.

### Preparation of MOFSNC by a nanoconfined interfacial growth strategy

A facilitated interfacial growth strategy was developed to assemble  $\text{UiO-66}-(\text{COOH})_2$  into an ethanediamine-modified PET NC (denoted as PET@EDA NC; see note S1 and fig. S1 for more information). One PET@EDA NC was clamped by a homemade interfacial synthesis apparatus consisting of two cells, one of which was filled with 5 ml of  $\text{ZrCl}_4$  (0.35 g) solution, and the other side was filled with 5 ml of  $\text{H}_4\text{BTEC}$  (0.38 g) solution, both solutions were preheated to  $90^\circ\text{C}$ . The interfacial synthesis equipment was then quickly sealed into a polytetrafluoroethylene (PTFE)-lined autoclave and transferred into a preheated oven at  $100^\circ\text{C}$  and maintained for 48 h. When the interfacial synthesis ended, the obtained  $\text{UiO-66}-(\text{COOH})_2$ -MOFSNC was taken out, washed with distilled water, and lastly dried at room temperature.

### Preparation of biomimetic sodium channels (15C5-MOFSNCs)

Sixty milligrams of  $N$ -(3-dimethylaminopropyl)- $N'$ -ethylcarbodiimide hydrochloride, 12 mg of  $N$ -hydroxysulfosuccinimide

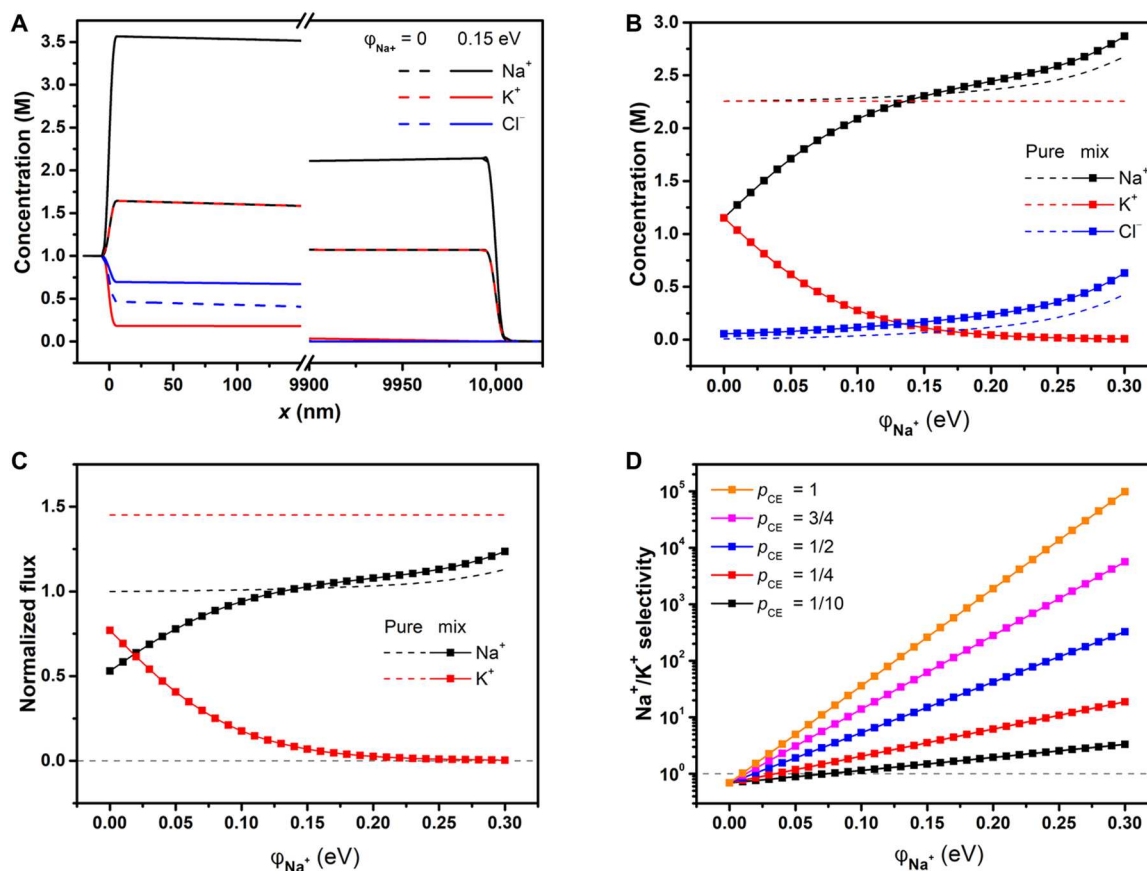


**Fig. 7. Theoretical simulations of  $\text{Na}^+/\text{K}^+$  selectivity in the 15C5-MOFSNC.** (A) Calculated ion concentrations in 1D model for the 15C5-SNC system MOFSNC for mixture ion permeation experiment using the mPNP theory (Materials and Methods). When the binding energy of 15C5 with  $\text{Na}^+$  is zero ( $\varphi_{\text{Na}^+} = 0$  eV), the cations  $\text{Na}^+$  and  $\text{K}^+$  have the same concentration. At  $\varphi_{\text{Na}^+} = 0.15$  eV, the preferable binding to 15C5 groups enhances the  $\text{Na}^+$  concentration. The markedly dropped  $\text{K}^+$  concentration should be attributed to electrostatic repulsion from the adsorbed  $\text{Na}^+$  ions. (B) The average  $\text{Na}^+$  and  $\text{K}^+$  concentration in the 15C5-MOFSNC channel as a function of  $\varphi_{\text{Na}^+}$  for both pure (i.e., single component) and mixed (i.e., multi-component) ion permeation cases. (C) The dependence of ion fluxes on  $\varphi_{\text{Na}^+}$ . The fluxes are normalized to that of  $\text{Na}^+$  in the single-component 1 M NaCl solution at  $\varphi_{\text{Na}^+} = 0$ . The relative order of  $\text{Na}^+$  and  $\text{K}^+$  fluxes is inverted for the mixture ion permeation case compared with the single-ion permeation case, which is consistent with experimental results. (D) The calculated  $\text{Na}^+/\text{K}^+$  selectivity increased with the increase of  $\varphi_{\text{Na}^+}$  and 15C5 density. Note that the dashed vertical line in (B) represents the lower limit of  $\varphi_{\text{Na}^+}$  values in experiments via our analysis.

sodium salt, and 20 mg of 15C5 were dissolved in 4 ml of Milli-Q water and filled into the two PTFE cells that clamped a UiO-66-(COOH)<sub>2</sub>-MOFSNC film. A transmembrane forward voltage of 1 V was applied to the tip side of MOFSNCs with a Pt electrode for 30 min. After that, the equipment was placed in the dark overnight, and then, the prepared 15C5-MOFSNC was taken out, washed with Milli-Q water, and lastly dried at room temperature.

### I-V characteristic measurement

The ionic transport properties of both NC and SNC membranes were studied by measuring *I-V* curves. Ionic currents were measured by a Keithley picoammeter (Keithley Instruments, Cleveland) on two PTFE chambers, which were separated by either a piece of PET NC film or a MOFSNC membrane. The two chambers were filled with chloride salt solutions at the same concentration. Ag/AgCl electrodes were used to apply a transmembrane potential across them. The forward voltage corresponded to the potential being applied on the base side. The main transmembrane potential used in this work was a scanning voltage varying from  $-2$  to  $+2$

V. In this work, each test was repeated at least three times to obtain the average current values at different voltages.

### Ion permeation experiments

The MOFSNC or 15C5-MOFSNC membrane was clamped between two PTFE compartments, of which one cell, facing the base side of the SNC membrane, was filled with 10 ml of salt solution as the feed, while the other side, facing the tip side of the SNC membrane was filled with 10 ml of Milli-Q water as the permeate side. For the single-ion permeation experiments, the feed solution was 10 ml of 1.0 M LiCl, 1.0 M NaCl, or 1.0 M KCl, while for the mixed ion permeation experiments, the feed was 10 ml of mixed ion solution containing 1.0 M LiCl, 1.0 M NaCl, and 1.0 M KCl. The constant voltage bias ranging from 0.25 to 4.0 V was applied in the feed side for 24 hours using Pt electrodes via a Keithley picoammeter across the membrane, with both compartments magnetically stirred gently. At the end of the experiments, the ion concentrations in the permeate side were measured by ICP-OES/MS. Permeation rate and permeability ratio values were calculated to evaluate the monovalent metal ion transport property in the MOFSNC and

15C5-MOFSNC membranes. The device area of  $2.83 \times 10^{-5} \text{ m}^2$  was used to calculate the ion permeate rates.

### Simulation methods

To gain molecular-level insights and lay the foundation for continuum modeling, MD simulations were carried out to understand the interactions of electrolyte ions with 15C5 inside or outside the MOF. The details of the MD simulation, including force fields, molecular models, simulation setup, and simulation code, are presented in the Supplementary Materials ("Theoretical simulations" section in note S2). The MD simulations were used to study the energetic preference of 15C5 in UiO-66-(COOH)<sub>2</sub>, selective adsorption of Na<sup>+</sup> over K<sup>+</sup> at 15C5 confined in UiO-66-(COOH)<sub>2</sub>, and the cavity blockage arising from the partial hydrated Na<sup>+</sup>@15C5 complex.

DFT calculations were also performed to confirm several key parameters predicted from MD simulations. The calculations were performed using the Vienna Ab initio Simulation Package version 6.3.1. The Perdew-Burke-Ernzerhof exchange-correlation functional (48) and the projector-augmented wave method (49) were adopted. To describe the long-range van der Waals interactions, the D3 correction proposed by Grimme and colleagues (50, 51) was used. The cutoff energy for the plane-wave basis set was selected as 400 eV. Gamma-only *k*-points mesh was used to sample the Brillouin zone of the supercells. The convergence criterion for the self-consistency process is set to  $10^{-6}$  eV to optimize the wave function. The structures were relaxed until the norms of all forces are smaller than 0.05 eV/Å.

To understand the experiment results, a 1D model is proposed for the 15C5-MOFSNC system. The widely used mPNP theory was adopted (46, 52, 53). The finite-element method implemented in the commercial COMSOL software was used to solve the equations. To account for both the electrostatic adsorption by the deprotonated -COOH (i.e., negatively charged background) and specific binding by 15C5 functional groups, we further modify the mPNP model as follows

$$\frac{\partial n_i}{\partial t} = D_i \nabla^2 n_i + n_i \mu_i \nabla (z_i e \phi + \Psi_i) + \frac{D_i n_i \nabla (n_{\text{Na}^+} + n_{\text{K}^+} + n_{\text{Cl}^-})}{n_{\text{MAX}} - (n_{\text{Na}^+} + n_{\text{K}^+} + n_{\text{Cl}^-})} \quad (1)$$

$$\epsilon \epsilon_0 \nabla^2 \phi = F(n_{\text{Na}^+} + n_{\text{K}^+} - n_{\text{Cl}^-} - n_{\text{MOF}}) \quad (2)$$

where Eq. 1 is the modified Nernst-Planck equation and  $n_i$  and  $z_i$  are the corresponding concentrations and valence number for  $i$ th ions (i.e., Na<sup>+</sup>, K<sup>+</sup>, and Cl<sup>-</sup>).  $n_{\text{MOF}}$  is the "concentration" of deprotonated -COOH groups in MOFSNC, namely, the amount of cation adsorbed into the MOFSNC in equilibrium. The first term is the classic Fick's second law for mass diffusion. The second one is the flux under the external driving force, (i.e., electric potential,  $\phi$ , and specific binding for the  $i$ th ion,  $\Psi_i$ ). It is noted that only the specific binding of Na<sup>+</sup> is accounted for (i.e., only  $\Psi_{\text{Na}^+} \neq 0$ ). The third term, also known as the entropy term, is the size constraint derived from the lattice gas model (53, 54). Here, the mPNP model is simplified by treating all kinds of ions with equal diameter,  $a = 0.66 \text{ nm}$  (46, 52).  $n_{\text{MAX}}$  is the maximum accessible concentration by  $n_{\text{MAX}} \approx 1/a^3 = 5.77 \text{ M}$ .

Equation 2 is the Poisson's equation, where  $\epsilon$ ,  $\epsilon_0$ ,  $F$ , and  $e$  are the relative permittivities, vacuum permittivity, Faraday constant, and elementary charges, respectively.  $\epsilon$  is set to be the bulk value in all regions. The drop in  $\epsilon$  in the MOFSNC region was found to enhance the nonspecific cation adsorption but had negligible effects on decreasing the selectivity (fig. S20).  $D_i$  and  $\mu_i$  are the diffusivity and electromobility for the  $i$ th ion and are related via the Einstein relations,  $\mu_i = D_i/k_B T$  with  $T = 300 \text{ K}$  and  $k_B$  as the Boltzmann constant.

Figure 4A illustrates the dimensions of our 1D mPNP model. To resemble the experimental setup, the 10- $\mu\text{m}$  length of 15C5-MOFSNC was sandwiched between two reservoirs with lengths  $L_R$  and  $L_{R'}$ . The concentration and electric potential gradient constraints,  $\Delta n \approx 1 \text{ M}$  and  $\Delta \phi = 1 \text{ V}$  were then set on the boundary of the two reservoirs. We examined the influence of  $L_R$  and  $L_{R'}$  values on Na<sup>+</sup>/K<sup>+</sup> selectivity results in figs. S16 and S17 and then adopted  $L_R = 20 \text{ nm}$  and  $L_{R'} = 90 \text{ nm}$  in this work.

In addition, it has been reported that the ion diffusivities inside the UiO-66-(COOH)<sub>2</sub> are several orders of magnitude lower than those in bulk solution (32). Thus, the diffusivity in the MOF region was roughly scaled down by the same magnitude  $H_{\text{MOF}}$  as  $D_i^{\text{MOF}} = D_i^0/H_{\text{MOF}}$  where  $D_i^0$  is the bulk diffusivity in the reservoirs. The  $D_i^0$  values of Na<sup>+</sup>, K<sup>+</sup>, and Cl<sup>-</sup> are set to be 13.5, 19.6, and 20.3 [ $10^{-6} \text{ cm}^2/\text{s}$ ], respectively. We set  $H_{\text{MOF}}$  to 100. The diffusivity of the monovalent ions is always in the order of  $D_{\text{K}^+} > D_{\text{Na}^+}$ , which reproduces the higher K<sup>+</sup> flux under single-component conditions. It was found that the ion selectivity would be slightly increased with the drop of  $H_{\text{MOF}}$  in fig. S21.

To model the 15C5-MOFSNC, we describe the distribution of 15C5 and -COOH groups in the MOF channel using two distribution functions  $p_{15\text{C5}}(x)$  and  $p_{\text{COOH}}(x)$  as illustrated in Fig. 4A. Note that  $p_{\text{COOH}} = 1$  means the maximum composition of -COOH groups in MOF, i.e., 48 groups per unit cell. In experiments, the 15C5 groups were grafted onto the -COOH groups (the condensation reaction with 15C5 decreased the number of -COOH groups); thus,  $p_{15\text{C5}}(x) + p_{\text{COOH}}(x) = 1$ . In this work, we adopted a trapezoidal distribution function for 15C5 groups. On the permeate end,  $p_{15\text{C5}}(L_{\text{MOF}}) = 8/48$ . This corresponds to one 15C5 group in each cavity of the UiO-66-(COOH)<sub>2</sub> framework. Owing to the large size of the 15C5 group, it is reasonable that 8/48 could be the maximum composition of 15C5 groups. Accordingly, we examined the influences of the ratio between the feed and permeation ends,  $p(0)/p(L_{\text{MOF}})$ , on the ion selectivity in our simulation and the results are presented in Fig. 3E.

Hence, the preferred binding of Na<sup>+</sup> is described as  $\Psi_{\text{Na}^+}(x) = -\varphi_{\text{Na}^+} \times \hat{p}_{15\text{C5}}(x)$ , where  $\varphi_{\text{Na}^+}$  is the binding strength of Na<sup>+</sup> and  $\hat{p}_{15\text{C5}}(x)$  is a normalized distribution function in which  $\hat{p}_{15\text{C5}}(L_{\text{MOF}}) = 1$ . As the -COOH groups would be deprotonated, the green curve of  $p_{\text{COOH}}(x)$  shows the profile of the negatively charged background (Fig. 4A). Thus,  $n_{\text{MOF}}(x) = n_{\text{MOF}}^0 p_{\text{COOH}}(x)$ , where  $n_{\text{MOF}}^0 = 2.57 \text{ M}$  is the equilibrium cation concentration in the pristine crystal to balance the negative background (32). The influences of other key parameters, such as the channel geometry, dielectric constant,  $n_{\text{MOF}}^0$ , and electrostatic potential gradient on the ion flux and ion selectivity, are discussed in detail in note S2.2 and figs. S15 to S21.

## Supplementary Materials

## This PDF file includes:

Supplementary Text

Figs. S1 to S23

Tables S1 and S2

References

## REFERENCES AND NOTES

- B. Hille, *Ionic Channels of Excitable Membranes* (Sinauer Associates Inc., ed. 3, 2001).
- T. Dudev, C. Lim, Factors governing the Na<sup>+</sup> vs K<sup>+</sup> selectivity in sodium ion channels. *J. Am. Chem. Soc.* **132**, 2321–2332 (2010).
- D. A. Doyle, J. M. Cabral, R. A. Pfuetzner, A. L. Kuo, J. M. Gulbis, S. L. Cohen, B. T. Chait, R. MacKinnon, The structure of the potassium channel: Molecular basis of K<sup>+</sup> conduction and selectivity. *Science* **280**, 69–77 (1998).
- Y. Zhou, J. H. Morais-Cabral, A. Kaufman, R. MacKinnon, Chemistry of ion coordination and hydration revealed by a K<sup>+</sup> channel–Fab complex at 2.0 Å resolution. *Nature* **414**, 43–48 (2001).
- E. Gouaux, R. MacKinnon, Principles of selective ion transport in channels and pumps. *Science* **310**, 1461–1465 (2005).
- T. Dudev, C. Lim, Ion selectivity strategies of sodium channel selectivity filters. *Acc. Chem. Res.* **47**, 3580–3587 (2014).
- L. Bocquet, Nanofluidics coming of age. *Nat. Mater.* **19**, 254–256 (2020).
- A. Legrand, S. Furukawa, A selective ionic rectifier. *Nat. Mater.* **19**, 701–702 (2020).
- R. Epsztein, R. M. DuChanois, C. L. Ritt, A. Noy, M. Elimelech, Towards single-species selectivity of membranes with subnanometre pores. *Nat. Nanotechnol.* **15**, 426–436 (2020).
- J. Lu, H. Wang, Emerging porous framework material-based nanofluidic membranes toward ultimate ion separation. *Matter* **4**, 2810–2830 (2021).
- T. M. Fyles, Synthetic ion channels in bilayer membranes. *Chem. Soc. Rev.* **36**, 335–347 (2007).
- J. Gao, Y. Feng, W. Guo, L. Jiang, Nanofluidics in two-dimensional layered materials: Inspirations from nature. *Chem. Soc. Rev.* **46**, 5400–5424 (2017).
- R. M. DuChanois, C. J. Porter, C. Violet, R. Verduzco, M. Elimelech, Membrane materials for selective ion separations at the water-energy nexus. *Adv. Mater.* **33**, 2101312 (2021).
- G. W. Gokel, S. Negin, Synthetic ion channels: From pores to biological applications. *Acc. Chem. Res.* **46**, 2824–2833 (2013).
- M. Tagliacruzchi, I. Szeifer, Transport mechanisms in nanopores and nanochannels: Can we mimic nature? *Mater. Today* **18**, 131–142 (2015).
- M. Barboiu, Encapsulation versus self-aggregation toward highly selective artificial K<sup>+</sup> channels. *Acc. Chem. Res.* **51**, 2711–2718 (2018).
- J. A. Vance, N. K. Devaraj, Membrane mimetic chemistry in artificial cells. *J. Am. Chem. Soc.* **143**, 8223–8231 (2021).
- Z. Sun, A. Gilles, I. Kocsis, Y. M. Legrand, E. Petit, M. Barboiu, Squallyl crown ether self-assembled conjugates: An example of highly selective artificial K<sup>+</sup> channels. *Chem. A Eur. J.* **22**, 2158–2164 (2016).
- E. T. Acar, S. F. Buchsbaum, C. Combs, F. Fornasiero, Z. S. Siwy, Biomimetic potassium-selective nanopores. *Sci. Adv.* **5**, eaav2568 (2019).
- F. Chen, J. Shen, N. Li, A. Roy, R. Ye, C. Ren, H. Zeng, Pyridine/oxadiazole-based helical foldamer ion channels with exceptionally high K<sup>+</sup>/Na<sup>+</sup> selectivity. *Angew. Chem. Int. Ed.* **59**, 1440–1444 (2020).
- Y. J. Jeon, H. Kim, S. Jon, N. Selvapalam, D. H. Oh, I. Seo, C.-S. Park, S. R. Jung, D.-S. Koh, K. Kim, Artificial ion channel formed by cucurbit [n] uril derivatives with a carbonyl group fringed portal reminiscent of the selectivity filter of K<sup>+</sup> channels. *J. Am. Chem. Soc.* **126**, 15944–15945 (2004).
- E. M. Choy, D. F. Evans, E. Cussler, Selective membrane for transporting sodium ion against its concentration gradient. *J. Am. Chem. Soc.* **96**, 7085–7090 (1974).
- O. Lawal, K. S. Iqbal, A. Mohamadi, P. Razavi, H. T. Dodd, M. C. Allen, S. Siddiqui, F. Cucuzzi, P. J. Cragg, An artificial sodium ion channel from calix[4]arene in the 1,3-alternate conformation. *Supramol. Chem.* **21**, 55–60 (2009).
- C. Ren, J. Shen, H. Zeng, Combinatorial evolution of fast-conducting highly selective K<sup>+</sup>-channels via modularly tunable directional assembly of crown ethers. *J. Am. Chem. Soc.* **139**, 12338–12341 (2017).
- R. Ye, C. Ren, J. Shen, N. Li, F. Chen, A. Roy, H. Zeng, Molecular ion fishers as highly active and exceptionally selective K<sup>+</sup> transporters. *J. Am. Chem. Soc.* **141**, 9788–9792 (2019).
- H. Furukawa, K. E. Cordova, M. O’Keeffe, O. M. Yaghi, The chemistry and applications of metal-organic frameworks. *Science* **341**, 1230444 (2013).
- A. J. Howarth, Y. Liu, P. Li, Z. Li, T. C. Wang, J. T. Hupp, O. K. Farha, Chemical, thermal and mechanical stabilities of metal-organic frameworks. *Nat. Rev. Mater.* **1**, 15018 (2016).
- J. Hou, H. Zhang, G. P. Simon, H. Wang, Polycrystalline advanced microporous framework membranes for efficient separation of small molecules and ions. *Adv. Mater.* **32**, e1902009 (2020).
- H. Zhang, J. Hou, Y. Hu, P. Wang, R. Ou, L. Jiang, J. Z. Liu, B. D. Freeman, A. J. Hill, H. Wang, Ultrafast selective transport of alkali metal ions in metal organic frameworks with subnanometer pores. *Sci. Adv.* **4**, eaaq0066 (2018).
- H.-Q. Liang, Y. Guo, X. Peng, B. Chen, Light-gated cation-selective transport in metal-organic framework membranes. *J. Mater. Chem. A* **8**, 11399–11405 (2020).
- Y. Guo, Y. Ying, Y. Mao, X. Peng, B. Chen, Polystyrene sulfonate threaded through a metal-organic framework membrane for fast and selective lithium-ion separation. *Angew. Chem. Int. Ed.* **55**, 15120–15124 (2016).
- J. Lu, H. Zhang, J. Hou, X. Li, X. Hu, Y. Hu, C. D. Easton, Q. Li, C. Sun, A. W. Thornton, M. R. Hill, X. Zhang, G. Jiang, J. Z. Liu, A. J. Hill, B. D. Freeman, L. Jiang, H. Wang, Efficient metal ion sieving in rectifying subnanochannels enabled by metal-organic frameworks. *Nat. Mater.* **19**, 767–774 (2020).
- J. Lu, H. Zhang, X. Hu, B. Qian, J. Hou, L. Han, Y. Zhu, C. Sun, L. Jiang, H. Wang, Ultraselective monovalent metal ion conduction in a three-dimensional sub-1 nm nanofluidic device constructed by metal-organic frameworks. *ACS Nano* **15**, 1240–1249 (2021).
- J. Abraham, K. S. Vasu, C. D. Williams, K. Gopinadhan, Y. Su, C. T. Cherian, J. Dix, E. Prestat, S. J. Haigh, I. V. Grigorieva, Tunable sieving of ions using graphene oxide membranes. *Nat. Nanotechnol.* **12**, 546–550 (2017).
- P. Wang, M. Wang, F. Liu, S. Ding, X. Wang, G. Du, J. Liu, P. Apel, P. Kluth, C. Trautmann, Ultrafast ion sieving using nanoporous polymeric membranes. *Nat. Commun.* **9**, 569 (2018).
- R. Tan, A. Wang, R. Malpass-Evans, E. W. Zhao, T. Liu, C. Ye, X. Zhou, B. P. Darwich, Z. Fan, L. Turcani, E. Jackson, L. Chen, S. Y. Chong, T. Li, K. E. Jelfs, A. I. Cooper, N. P. Brandon, C. P. Grey, N. B. McKeown, Q. Song, Hydrophilic microporous membranes for selective ion separation and flow-battery energy storage. *Nat. Mater.* **19**, 195–202 (2019).
- J. Lu, X. Hu, K. M. Ung, Y. Zhu, X. Zhang, H. Wang, Metal-organic frameworks as a subnanometer platform for ion-ion selectivity. *Acc. Mater. Res.* **3**, 735–747 (2022).
- X. Hou, *Bio-inspired Asymmetric Design and Building of Biomimetic Smart Single Nanochannels* (Springer Science & Business Media, 2013).
- G. C. Shearer, S. Chavan, S. Bordiga, S. Svella, U. Olsbye, K. P. Lillerud, Defect engineering: Tuning the porosity and composition of the metal-organic framework UiO-66 via modulated synthesis. *Chem. Mater.* **28**, 3749–3761 (2016).
- Q. Y. Yang, S. Vaesen, F. Ragon, A. D. Wiersum, D. Wu, A. Lago, T. Devic, C. Martineau, F. Taulelle, P. L. Llewellyn, H. Jobic, C. L. Zhong, C. Serre, G. De Weireld, G. Maurin, A water stable metal-organic framework with optimal features for CO<sub>2</sub> capture. *Angew. Chem. Int. Ed.* **52**, 10316–10320 (2013).
- S. J. Warnock, R. Sujjanani, E. S. Zofchak, S. Zhao, T. J. Dilenschneider, K. G. Hanson, S. Mukherjee, V. Ganesan, B. D. Freeman, M. M. Abu-Omar, Engineering Li/Na selectivity in 12-crown-4-functionalized polymer membranes. *Proc. Natl. Acad. Sci. U.S.A.* **118**, e2022197118 (2021).
- N. Shi, S. Ye, A. Alam, L. Chen, Y. Jiang, Atomic structure of a Na<sup>+</sup>- and K<sup>+</sup>-conducting channel. *Nature* **440**, 570–574 (2006).
- C. Shi, Y. He, K. Hendriks, B. L. de Groot, X. Cai, C. Tian, A. Lange, H. Sun, A single nak channel conformation is not enough for non-selective ion conduction. *Nat. Commun.* **9**, 1–8 (2018).
- G. Hummer, Potassium ions line up. *Science* **346**, 303 (2014).
- D. A. Köpfer, C. Song, T. Gruene, G. M. Sheldrick, U. Zachariae, B. L. de Groot, Ion permeation in K<sup>+</sup> channels occurs by direct coulomb knock-on. *Science* **346**, 352–355 (2014).
- C. Cheng, G. Jiang, C. J. Garvey, Y. Wang, G. P. Simon, J. Z. Liu, D. Li, Ion transport in complex layered graphene-based membranes with tuneable interlayer spacing. *Sci. Adv.* **2**, e1501272 (2016).
- J. Guo, J. Lee, C. I. Contescu, N. C. Gallego, S. T. Pantelides, S. J. Pennycook, B. A. Moyer, M. F. Chisholm, Crown ethers in graphene. *Nat. Commun.* **5**, 1–6 (2014).
- J. P. Perdew, K. Burke, M. Ernzerhof, Generalized gradient approximation made simple. *Phys. Rev. Lett.* **77**, 3865–3868 (1996).
- G. Kresse, D. Joubert, From ultrasoft pseudopotentials to the projector augmented-wave method. *Phys. Rev. B* **59**, 1758–1775 (1999).
- S. Grimme, J. Antony, S. Ehrlich, H. Krieg, A consistent and accurate ab initio parametrization of density functional dispersion correction (DFT-D) for the 94 elements H-PU. *J. Chem. Phys.* **132**, 154104 (2010).
- J. Moellmann, S. Grimme, Importance of london dispersion effects for the packing of molecular crystals: A case study for intramolecular stacking in a bis-thiophene derivative. *Phys. Chem. Chem. Phys.* **12**, 8500–8504 (2010).
- C. Cheng, G. Jiang, G. P. Simon, J. Z. Liu, D. Li, Low-voltage electrostatic modulation of ion diffusion through layered graphene-based nanoporous membranes. *Nat. Nanotechnol.* **13**, 685–690 (2018).

53. Y. Huang, X. Liu, S. Li, T. Yan, Development of mean-field electrical double layer theory. *Chin. Phys. B* **25**, 016801 (2016).
54. A. A. Kornyshev, Double-layer in ionic liquids: Paradigm change? *J. Phys. Chem. B* **111**, 5545–5557 (2007).
55. P. G. Boyd, S. M. Moosavi, M. Witman, B. Smit, Force-field prediction of materials properties in metal-organic frameworks. *J. Phys. Chem. Lett.* **8**, 357–363 (2017).
56. A. K. Rappé, C. J. Casewit, K. Colwell, W. A. Goddard III, W. M. Skiff, UFF, a full periodic table force field for molecular mechanics and molecular dynamics simulations. *J. Am. Chem. Soc.* **114**, 10024–10035 (1992).
57. A. K. Rappe, W. A. Goddard III, Charge equilibration for molecular dynamics simulations. *J. Phys. Chem.* **95**, 3358–3363 (1991).
58. E. S. Kadantsev, P. G. Boyd, T. D. Daff, T. K. Woo, Fast and accurate electrostatics in metal organic frameworks with a robust charge equilibration parameterization for high-throughput virtual screening of gas adsorption. *J. Phys. Chem. Lett.* **4**, 3056–3061 (2013).
59. J.-P. Ryckaert, G. Ciccotti, H. J. Berendsen, Numerical integration of the cartesian equations of motion of a system with constraints: Molecular dynamics of n-alkanes. *J. Comput. Phys.* **23**, 327–341 (1977).
60. S. Plimpton, Fast parallel algorithms for short-range molecular dynamics. *J. Comput. Phys.* **117**, 1–19 (1995).
61. D. Ongari, P. G. Boyd, S. Barthel, M. Witman, M. Haranczyk, B. Smit, Accurate characterization of the pore volume in microporous crystalline materials. *Langmuir* **33**, 14529–14538 (2017).
62. J. Son, T. Takami, J.-K. Lee, T. Kawai, B. Park, Concentration dependence of ionic conductance measured with ion-selective sub-micro pipette probes in aqueous sodium and potassium chloride solutions. *Appl. Phys. Lett.* **99**, 033701 (2011).
63. T. Ye, G. Hou, W. Li, C. Wang, K. Yi, N. Liu, J. Liu, S. Huang, J. Gao, Artificial sodium-selective ionic device based on crown-ether crystals with subnanometer pores. *Nat. Commun.* **12**, 1–8 (2021).
64. E. R. Nightingale, Phenomenological theory of ion solvation. Effective radii of hydrated ions. *J. Phys. Chem.* **63**, 1381–1387 (1959).
65. Y. Marcus, A simple empirical model describing the thermodynamics of hydration of ions of widely varying charges, sizes, and shapes. *Biophys. Chem.* **51**, 111–127 (1994).

**Acknowledgments:** We acknowledge the use of instruments and scientific and technical assistance at the Monash Centre for Electron Microscopy, a Node of Microscopy Australia. Part of the XRD experiments was performed at the powder diffraction beamline, Australian Synchrotron (ANSTO). The used PET films are part of a UMAT experiment, which was performed at the beamline X0 at the GSI Helmholtzzentrum für Schwerionenforschung, Darmstadt (Germany) in the frame of FAIR Phase-0. J.Z.L. acknowledges the support of the HPC Facility from the National Computational Infrastructure in Australia. G.J. thanks the National Natural Science Foundation of China (grant no. 21905215) for financial support. **Funding:** The authors thank the Australian Research Council (FL200100049, DP180100298, DE170100006, DP170102964, and DP180102890) for the financial support. H.W. is the recipient of an Australian Research Council Australian Laureate Fellowship (FL200100049). H.Zhang. is the recipient of an Australian Research Council Future Fellowship (FT200100259). **Author contributions:** H.Zha. conceived the project idea. H.W. and H.Zha. supervised the project. J.L. designed the experiments with supervision from H.W. and H.Zha. J.L. conducted the sample preparation, measurements, and characterizations. G.J. and Y.Y. conducted the simulations and modeling under the guidance of J.Z.L. B.Q. helped conduct the ICP-OES/MS measurements. H. Zhu performed the NMR characterization. Q.G. performed the synchrotron XRD characterization. J.L. wrote the manuscript with input from G.J. and H.Zha. H.W., J.L., H.Zha., J.Z.L., G.J., B.D.F., and L.J. revised the manuscript. All authors contributed to the data analysis and discussion. **Competing interests:** The authors declare that they have no competing interests. **Data and materials availability:** All data needed to evaluate the conclusions in the paper are present in the paper and/or the Supplementary Materials.

Submitted 21 March 2022  
Accepted 23 December 2022  
Published 27 January 2023  
10.1126/sciadv.abq1369